Instability of Dynamic Localization in Intense THz-Driven Semiconductor Wannier-Stark Ladder due to Dynamic Fano Resonance

Atsushi Kukuu, Tomohiro Amano, Tomohiro Karasawa, Nobuya Maeshima, and Ken-ichi Hino*

Doctoral Program in Frontier Science,

Graduate School of Pure and Applied Sciences, University of Tsukuba,

1-1-1 Tennodai, Tsukuba, Ibaraki 305-8573, Japan

(Dated: August 23, 2010)

Abstract

The lifetime of an electronic Floquet state in a semiconductor Wannier-Stark ladder (WSL) driven by an intense monochromatic THz wave is examined based on the R-matrix Floquet theory, in which an excess density of state (DOS) corresponding to the lifetime is calculated. It is revealed that the dynamic localization (DL) characteristic of this system is unstable against Fano resonance (FR)-like inter-miniband decay mechanism caused by THz-mediated ac-Zener tunneling; in this study, this is termed as dynamic Fano resonance (DFR). The DFR is considered to be a new FR mechanism characterized by both tunable ac-ZT coupling and coexistence with shape resonance. The result obtained here is in sharp contrast with the conventional understanding without the introduction of DFR, in which the DL is very stable such that its lifetime is comparable to or greater than that of the associated WSL. It is found that the DFR mechanism generally becomes more dominant with an increase in the strength of the bias field. Further, we discuss the observation that the spectral pattern of the excess DOS is more involved for a single-photon resonant transition, namely, $\Omega = \omega$, than that for a two-photon resonant transition, namely, $\Omega = 2\omega$, where Ω and ω represent a Bloch frequency and a THz frequency, respectively. In addition, the criterion for the applicability of the DFR to the present system is also obtained.

PACS numbers: 78.67.Pt,42.50.Hz

*Electronic address: hino@bk.tsukuba.ac.jp

I. INTRODUCTION

The advent of inexpensive intense THz light sources such as molecular THz lasers and free-electron lasers [1] has enabled innovative research in the areas of high-power THz excitation of semiconductors and the relevant coherent control of quantum dynamics [2]. A THz wave having a peak intensity of the order of hundreds of kV/cm has recently been demonstrated using a pulsed laser [3, 4]. It has been found that the irradiation of a periodically oscillating THz wave causes photon-mediated tunneling in quantum wells (QWs), superlattices (SLs), and Wannier-Stark ladders (WSLs). In particular, the application of an appropriately controlled periodic drive to these systems brings quantum transport and diffusion to an almost complete stop [5]. In THz-driven SLs and WSLs, the latter of which are also called as dynamic WSLs (DWSLs), such spatial localization, called as dynamic localization (DL), is characterized by the collapse of quasienergy minibands [6, 7]. It has been found that DL in the DWSL leads to the formation of sharp peaks in the optical spectra, and these are therefore more enhanced than or comparable to those in the corresponding WSL (without THz driving) [8, 9]. In addition, it is well known that the DWSL problem is analogous to the Hofstadter problem for the energy spectra of a Bloch electron under a static magnetic field [10]. In asymmetric double QWs, the phenomenon termed coherent destruction of tunneling has been discussed [11, 12], in which tunneling is destroyed in a manner similar to that by DL, and further its relation with DL is understood from the viewpoint of group theory and the Landau-Zener problem [13]. Further, DL has been discussed in double-quantum-dot molecules [14] and one-dimensional lattices under the influence of ac electric and magnetic fields [15].

In addition to semiconductor systems, DL has also been extensively studied from the viewpoint of driven quantum tunneling and coherent control in systems such as optical SLs [16], atomic hyperfine and Zeeman-level structures [17–19], spin systems [20], and quantum chaos [21]. Further the concept of DL has recently been extended to trapped atoms in Bose-Einstein condensates [22], Cooper pairs in Josephson qubits [23], and correlated electron systems [24].

In this study, we focus on DL from the viewpoint of its stability in the intense region of the THz field. To the best of our knowledge, there have been no studies on this issue except for Ref. [21]. According to some existing theoretical studies based on the lowest

two-miniband tight-binding model [25, 26], even if the strength of the THz wave (F_{ac}) increases, miniband collapse is still observed, although ac-Zener tunneling (ac-ZT) across photon sidebands (PSBs) corresponding to different minibands becomes more significant, and this results in pronounced anticrossings. Therefore, it is considered that DL would retain a stable Floquet state and would be only minimally affected by ac-ZT. However, as F_{ac} is enhanced to the intense region of the order of hundreds of kV/cm, it can be hypothesized that a large number of PSBs contribute to this coupling, invalidating the conventional interpretation mentioned above. Further, state-of-the-art THz light sources that can realize such intensities have already been produced [3, 4], as mentioned above.

Based on the ac-ZT-free Houston-Floquet picture [25, 26], quasienergies of a single-electron DWSL form a manifold structure labeled as (b, j), where b and j represent the indices of a miniband and a PSB, respectively. In particular, for the concerned DL, the (b, j) level is usually considered to be discrete. In fact, because of dc-Zener tunneling (dc-ZT) arising from an applied bias (with strength F_0), these DL levels would more or less incur shape resonance (SR) decay, although only the $(1, j)$ level can still be approximately considered to be discrete; the SR width broadens as b increases. Figure 1 shows the manifold structure of the DL levels, where each level is shaded, indicating the SR continuum. Here, it should be noted that because of ac-ZT coupling, the (approximately discrete) parent DL band of $(1, 0)$ with quasienergy E likely interacts with degenerate (SR-broadened) replicas of $(b > 1, j < 0)$, leading to instability. According to a simple perturbation picture, the parent band with $j = 0$ is believed to be predominantly coupled with an adjacent PSB with $|j| = 1$, and higher-order interactions with $|j| \geq 2$ generally assume greater importance with an increase in F_{ac}. Here, this new mechanism is termed dynamic Fano resonance (DFR) because it is similar to the conventional Fano effect [27] that arises from *static* couplings, for instance, an electron-electron interaction in a helium atom [28] and an electron-phonon coupling in a heavily doped p-type silicon crystal [29]. Unlike in the case of such static couplings, the strength of the ac-ZT coupling for the DFR can be tuned by changing F_{ac} and the THz frequency; in the present DWSL problem, the Bloch frequency is set to be equal to an integer multiple of the THz frequency. Therefore, it is believed that the DFR will provide a new possibility for the coherent control of both the spectral intensity and the profile in DWSL. In addition, the DFR effect is rather similar to the laser-induced continuum structure [30] that has recently been applied to strongly interacting Bose-Einstein

condensates in an ultracold atomic system as an optical Feshbach effect [31–33].

Considering the DFR, the DWSL problem reduces to a multichannel scattering (MCS) problem. In this study, the MCS states are numerically solved based on the R-matrix Floquet theory (RFT) [34], and we attempt to find a complete solution, namely, a non-approximated solution, for the single electron DWSL problem within numerical round-off inaccuracy. By evaluating the excess density of state (DOS) [35–38] of DWSL, it is demonstrated that the DL band $(1, 0)$ is really unstable in a certain region of THz intensity, as shown later. The excess DOS is an important physical quantity because it is associated with the lifetime of the concerned resonance state, and further, it provides the initial characterization for understanding a more complicated problem, for instance, the problem of the transient interband coherent dynamics of a THz-driven semiconductor DWSL. Obviously, the MCS problem in relation to DFR has not been adequately studied within the framework of the conventional tight-binding method.

Below, some recent investigations related to the present study are briefly described and the differences among them are clarified. First, in Ref. [21], the MCS problem of a fractional DWSL for modeled optical SLs, and not for semiconductor SLs, was analyzed by means of the Floquet-Bloch method. Quasienergy resonance structures were examined by solving the associated non-Hermitian eigenvalue problem with the Siegert boundary conditions, unlike in the present RFT method. However, this study did not focus on the DFR of DL states. Furthermore, the abovementioned Floquet-Bloch method is difficult to apply in its original form to the DWSL problem beyond a single-particle approximation because a Bloch momentum is no longer a good quantum number for more complicated problems, for example, of a DWSL exciton. In contrast, recently, the RFT method has been straightforwardly applied to the MCS problem of the THz-driven excitonic DWSL [39]. For the study of a DWSL exciton, Ref. [40] used the terminology of DFR in a different sense in which the THz wave was so weak that ac-ZT was of no importance, and hence, the Fano resonance (FR) was caused simply by a Coulomb interaction. In addition, the nonlinear Fano effect was discussed in semiconductor QWs and quantum dots in Refs. [41] and [42], respectively, where the FR arising from *static* couplings was probed in an optically nonlinear regime at high power. This is somewhat similar to laser-induced autoionization [43, 44], rather than to the abovementioned laser-induced continuum structure [30]. Finally, THz-driven excitonic spectra were recently studied in multiple QWs [45]. According to this, the excitonic resonance redshifts

and the absorption linewidth broadens because of the dynamic Franz-Keldysh effect that resembles the DWSL concerned here. In this report, the polarization direction of the THz wave is normal to the direction of crystal growth, and thus, the DL is not expected, unlike in the present study, in which the polarization is along this direction.

The remainder of this article is organized as follows. Sec. II describes the framework of the RFT. Sec. III presents the results and discussions. Finally, Sec. IV presents the conclusions. Atomic units (a.u.) are used throughout unless otherwise stated. All acronyms defined in this article are summarized in Tab. I.

II. THEORY

The RFT is introduced to the present DWSL problem in the following two subsections. In Sec. II A, the Floquet expansion based on the Kramers-Henneberger (KH) transformation [46] is presented, and the MCS equations to be solved are derived. In Sec. II B, the R-matrix propagation technique [47] for numerically solving these equations is introduced.

A. Floquet Expansion

Let us begin with the DWSL Hamiltonian

$$H(z,t) = \left[p_z + \frac{1}{c}A(t)\right] \frac{1}{m(z)} \left[p_z + \frac{1}{c}A(t)\right] + V(z), \tag{1}$$

where $V(z)$, $m(z)$, and p_z represent the SL confining potential, effective mass of an electron, and momentum operator along the crystal growth direction z, respectively, and $A(t)$ is a vector potential at time t for an applied electric field $F(t) = -\dot{A}(t)/c$, where c is the speed of light. Based on the RFT [34], the application of a gauge transformation and the KH transformation [46] to the DWSL wavefunction satisfying

$$\left[H(z,t) - i\frac{\partial}{\partial t}\right] \Psi(z,t) = 0 \tag{2}$$

yields the equation

$$\left[\mathcal{H}(z,t) - i\frac{\partial}{\partial t}\right] \Phi(z,t) = 0, \tag{3}$$

where

$$\mathcal{H}(z,t) = p_z \left[\frac{1}{m(z+a(t))}\right] p_z + V(z+a(t)) + F_0 z + v(z,t), \tag{4}$$

and $v(z,t)$ represents the residual part given by

$$v(z,t) = \frac{A_1(t)}{c}\left[\frac{1}{m(z+a(t))} - \frac{1}{m_\infty}\right] p_z + \frac{A_1(t)}{2c}\left\{p_z\left[\frac{1}{m(z+a(t))}\right]\right\} + \frac{1}{2}\left[\frac{1}{m(z+a(t))} - \frac{1}{m_\infty}\right]\left(\frac{A_1(t)}{c}\right)^2. \quad (5)$$

The successive transformation from Eq. (2) into Eq. (3) is explicitly expressed as

$$\Psi(z,t) = \exp\left[-if(z,t)\right]\exp\left[-ia(t)p_z\right]\Phi(z,t). \quad (6)$$

In Eq. (6), $f(z,t)$ for the gauge transformation and $a(t)$ for the KH transformation are given by

$$f(z,t) = \frac{A_0(t)}{c}(z+a(t)) + \frac{1}{2m_\infty}\int^t \left(\frac{A_1(t)}{c}\right)^2 dt \quad (7)$$

and

$$a(t) = \frac{1}{m_\infty}\int^t \frac{A_1(t)}{c} dt, \quad (8)$$

respectively. Here, $A(t) = A_0(t) + A_1(t)$, and a dc-electric field and a THz field are defined as $F_0 = -\dot{A}_0(t)/c$ and $F_1(t) = -\dot{A}_1(t)/c$, respectively. It should be noted that the KH transformation is considered to be a gauge transformation that is closely related to the acceleration form of an optical dipole interaction [48]. Further, it should be noted that $\mathcal{H}(z,t)$ becomes

$$\mathcal{H}_{as}(z) = \frac{p_z^2}{2m_\infty} + F_0 z + V_\infty, \quad (9)$$

and $v(z,t)$ vanishes in the asymptotic region of $|z+a(t)| >> 1$, where it has been assumed that $V(z+a(t))$ and $m(z+a(t))$ become the constant values of V_∞ and m_∞, respectively.

$\mathcal{H}(z,t)$ ensures the Floquet theorem, because we are concerned with monochromatic THz driving with $F_1(t) = F_{ac}\cos\omega t$, where ω is a frequency. Therefore, $\Phi(z,t)$ is expressed as

$$\Phi(z,t) = \exp\left(-iEt\right)\sum_{\nu=-N_{ph}}^{N_{ph}} \exp\left(i\nu\omega t\right)\psi_\nu(z), \quad (10)$$

and Eq. (3) is recast into the coupled equations

$$\sum_{\nu=-N_{ph}}^{N_{ph}} \left[L_{\mu\nu}(z) - E\delta_{\mu\nu}\right]\psi_\nu(z) = 0, \quad (11)$$

where $L_{\mu\nu}(z)$ is given by

$$L_{\mu\nu}(z) = \mathcal{H}_{\mu\nu}(z) + \mu\omega\delta_{\mu\nu} \quad (12)$$

with E representing a quasienergy and $N_{ph} >> 1$. Hereafter, it is understood that the time average of an arbitrary function $X(z,t)$ has been defined as

$$X_{\mu\nu}(z) = \frac{1}{T}\int_0^T \exp\left[-i(\mu-\nu)\omega t\right] X(z,t), \tag{13}$$

where $T = 2\pi/\omega$. It should be noted that $L_{\mu\nu}(z)$ becomes $L_{\mu}^{(as)}(z)\delta_{\mu\nu}$, where

$$L_{\mu}^{(as)}(z) = \mathcal{H}_{as}(z) + \mu\omega \tag{14}$$

in the region of $|z+\alpha| >> 1$. Here, α, defined as

$$\alpha = \frac{F_{ac}}{m_{\infty}\omega^2}, \tag{15}$$

is called the ponderomotive radius corresponding to the excursion amplitude of a classical electron traveling under $F_1(t)$.

For any E, open boundary conditions are imposed on $\{\psi_\nu(z)\}$ at $z = z_{as} < 0$ with $|z_{as}| >> 1$ because of $F_0 z_{as} + V_\infty + \nu\omega \to -\infty$. Hence, Eq. (11) is regarded as the coupled equations for the MCS problem, where an asymptotic scattering channel is provided by field-free solutions for Eq. (14), and this is designated by a photon index ν with $-N_{ph} \le \nu \le N_{ph}$. There exist M_{ph}-independent solutions composed of a set of the components $\{\psi_\nu(z)\}$ with $M_{ph} = 2N_{ph}+1$, because all channels are open. Thus, $\psi_\nu(z)$ is hereafter written as $\psi_{\nu\beta}(z)$ with $-N_{ph} \le \beta \le N_{ph}$ in order to specify the βth solution.

B. MCS Problem

In what follows, Eq. (11) is solved by employing the R-matrix propagation technique [47]. First, the scattering coordinate z is divided into N sectors, where the nth sector S_n is given as $[z_n, z_{n+1}]$ $(n = 1 \sim N)$ with $z_1 = z_{as}$ and $z_{N+1} = |z_{as}|$. Rewriting $L_{\mu\nu}(z)$ as

$$L_{\mu\nu}(z) = \mathcal{L}_{\mu\nu}(z) - B_{\mu\nu}(z), \tag{16}$$

Eq. (11) for $z \in S_n$ is read as

$$\sum_{\nu=-N_{ph}}^{N_{ph}} \left[\mathcal{L}_{\mu\nu}(z) - E\delta_{\mu\nu}\right]\psi_{\nu\beta}(z) = \sum_{\nu=-N_{ph}}^{N_{ph}} B_{\mu\nu}(z)\psi_{\nu\beta}(z), \tag{17}$$

where $\mathcal{L}_{\mu\nu}(z)$ is determined so as to be Hermitian in S_n, and thus, the Bloch operator $B_{\mu\nu}(z)$ is given by

$$B_{\mu\nu}(z) = [\delta(z-z_{n+1}) - \delta(z-z_n)]b_{\mu\nu}(z), \tag{18}$$

where

$$b_{\mu\nu}(z) = \left[\frac{1}{2m(z+a(t))}\right]_{\mu\nu} \frac{\partial}{\partial z} + i\left[\frac{A_1(t)}{2c}\left(\frac{1}{m(z+a(t))} - \frac{1}{m_\infty}\right)\right]_{\mu\nu}. \tag{19}$$

Next, the coupled equations

$$\sum_{\nu=-N_{ph}}^{N_{ph}} \left[\mathcal{L}_{\mu\nu}(z) - \varepsilon_k \delta_{\mu\nu}\right] \phi_{\nu k}(z) = 0 \tag{20}$$

are solved within S_n. In the practical numerical calculations for solving the eigenvalue problem of Eq. (20), the Legendre-type discrete variable representation [49] is employed as a piecewise basis set for the z-coordinate. Here, $\{\phi_{\nu k}(z)\}$ is the set of components of the kth eigenfunction with ε_k as the associated eigenvalue, and these functions are orthonormalized in S_n, namely,

$$\sum_{\nu} (\phi_{\nu k} | \phi_{\nu k'}) = \delta_{kk'}, \tag{21}$$

where $(\phi_{\nu k}|\phi_{\nu k'})$ implies an integration over S_n.

Expanding $\psi_{\nu\beta}(z)$ with respect to $\{\phi_{\nu k}(z)\}$ as

$$\psi_{\nu\beta}(z) = \sum_k \phi_{\nu k}(z) c_{k\beta}, \tag{22}$$

and putting it into Eq. (17), a set of the expansion coefficients is obtained as

$$c_{k\beta} = \sum_{\mu\nu} \frac{(\phi_{\mu k}|B_{\mu\nu}\psi_{\nu\beta})}{\varepsilon_k - E}. \tag{23}$$

Then, $\psi_{\mu\beta}(z)$ becomes of the form

$$\psi_{\mu\beta}(z) = \sum_{\nu\nu'} \left[G_{\mu\nu}(z, z_{n+1}) b_{\nu\nu'}(z_{n+1}) \psi_{\nu'\beta}(z_{n+1}) \; - G_{\mu\nu}(z, z_n) b_{\nu\nu'}(z_n) \psi_{\nu'\beta}(z_n)\right], \tag{24}$$

where the R-matrix Green function $G_{\mu\nu}(z, z')$ is defined as

$$G_{\mu\nu}(z, z') = \sum_k \frac{\phi_{\mu k}(z) \phi^*_{\nu k}(z')}{E - \varepsilon_k}. \tag{25}$$

Further, defining the R-matrix as

$$R_{\mu\nu}(z_i) = \sum_\beta \psi_{\mu\beta}(z_i) \left[b(z_i)\psi(z_i)\right]^{-1}_{\beta\nu}, \tag{26}$$

one obtains the relation between $R(z_n)$ and $R(z_{n+1})$ by employing Eq. (24) with the z set equal to z_n and z_{n+1}, as follows:

$$R(z_n) = G(z_n, z_n) - G(z_n, z_{n+1}) \frac{1}{G(z_{n+1}, z_{n+1}) + R(z_{n+1})} G(z_{n+1}, z_n), \tag{27}$$

where matrix notations have been used for the sake of simplicity. This expression enables one to calculate $R(z_n)$ by means of the propagators $G(z_i, z_j)$, once $R(z_{n+1})$ is known in advance. The successive application of this relation to every sector from S_N to S_1 provides $R(z_1)$, where the initial value of $R(z_{N+1})$ is given by the boundary condition imposed at $z = z_{N+1}$.

The scattering boundary condition

$$\psi_{\mu\beta}(z_1) = \chi_\mu^{(+)}(z_1)\delta_{\mu\beta} - \chi_\mu^{(-)}(z_1)S_{\mu\beta}(E) \tag{28}$$

is imposed on $\psi_{\mu\beta}(z_1)$, where $\chi_\mu^{(\pm)}(z)$ is the energy-normalized progressive wave in the direction of $\pm z$, satisfying

$$[L_\mu^{(as)}(z) - E]\chi_\mu^{(\pm)}(z) = 0 : \tag{29}$$

$\chi_\mu^{(\pm)}(z)$ is associated with the Airy function. The scattering matrix $S(E)$ is provided by matching the asymptotic boundary condition, given by

$$R_{\mu\nu}^{(as)}(z_1) = \sum_\beta \psi_{\mu\beta}(z_1)\left[b(z_1)\psi(z_i)\right]_{\beta\nu}^{-1}, \tag{30}$$

with $R(z_1)$ obtained by the R-matrix propagation procedure. In terms of a time-delay matrix provided by $S(E)$, namely,

$$\tau(E) = -i[S(E)]^{-1}\frac{dS(E)}{dE}, \tag{31}$$

an excess DOS is defined by

$$\rho^{(ex)}(E) = \mathrm{Tr}[\tau(E)], \tag{32}$$

and the lifetime of the concerned state with E is given by

$$T(E) = \frac{\mathrm{Tr}[\tau(E)]}{N_o}, \tag{33}$$

where N_o is the number of open channels [35–38]. The excess DOS is also expressed as

$$\rho^{(ex)}(E) = \rho(E) - \rho^{(as)}(E), \tag{34}$$

where $\rho(E)$ and $\rho^{(as)}(E)$ represent the DOS of the concerned DWSL and that of a field-free asymptotic state corresponding to $\chi_\mu^{(\pm)}(z)$, respectively. Because $\rho^{(as)}(E)$ exhibits only structureless continuum, the DFR structure observed in $\rho^{(ex)}(E)$ is considered to be almost similar to that in $\rho(E)$. There exists the periodicity

$$\rho^{(ex)}(E) = \rho^{(ex)}(E + k\omega), \tag{35}$$

where k is an integer, because of the relation

$$S_{\mu,\beta}(E) = S_{\mu+k,\beta+k}(E + k\omega). \tag{36}$$

III. RESULTS AND DISCUSSION

Beginning with the presentation of the setup parameters used in the actual calculations in Secs. III A, the basic understanding of ponderomotive interactions is shown along with the calculated results in Sec. III B. The excess DOSs with $n = 2$ and $n = 1$ are discussed in Secs. III C and III D, respectively. Further, the criteria for the applicability of the present DFR mechanism are discussed in Sec. III E.

A. Setup Parameters

The actual calculations are implemented for the SL of 35/11 ML GaAs/$Ga_{0.75}Al_{0.25}As$ (1 ML = 2.83 Å) with a lattice constant $d = 246$, where the effective masses of electrons in the well and barrier regions of the QW are $m_w = 0.0665$ and $m_b = 0.0772$, respectively, and the height of the confining QW potential is $V_b = 7.8 \times 10^{-3}$. The concerned SLs are designed to be composed of ten QWs in the range of $-5.5d \le z \le 4.5d$ that are surrounded by $Ga_{0.75}Al_{0.25}As$ in the regions beyond $z \le -5.5d$ and $z \ge 4.5d$. Hence, m_∞ and V_∞ are identical to m_b and V_b, respectively. In addition, $z_{as} = -2500$, $N = 1842$, and $N_{ph} = 20$ are adopted for the convergence of all of the calculated results.

Hereafter, we consider the case of $\Omega = n\omega$, where n is a positive integer and Ω is the Bloch frequency, given by $\Omega = F_0 d$. In Sec. III C, n is set to 2 and $\Omega = 5 \times 10^{-3}$ with $F_0 = 104.5$ kV/cm. Further, α is changed from 1 ($F_{ac} = 2.5$ kV/cm) to 108.2 ($F_{ac} = 268.4$ kV/cm). On the other hand, in Sec. III D, n is set equal to 1 and $\Omega = 2.5 \times 10^{-3}$ with $F_0 = 52.3$ kV/cm. It is well known that DL occurs when F_{ac} and ω satisfy the following relation that the matching ratio, given by

$$x_k^{(n)} = \frac{F_{ac} d}{\omega}, \tag{37}$$

is equal to the kth zero of the nth-order Bessel function of the first kind ($n \neq 0$) [7]. We have $x_1^{(1)} = 3.832$, $x_2^{(1)} = 7.016$, $x_1^{(2)} = 5.136$, and $x_2^{(2)} = 8.417$. Hereafter, it is understood that α corresponding to DL at $x_k^{(n)}$ is expressed as $\alpha_{DL}^{(n,k)}$.

B. Ponderomotive Interactions

Defining as

$$U_{\mu-\nu}(z) \equiv V_{\mu\nu}(z) + F_0 z\delta_{\mu\nu} \tag{38}$$

the ponderomotive interaction arising from the renormalization of the THz field to $V(z)$, $L_{\mu\nu}(z)$ is rewritten as

$$L_{\mu\nu}(z) = p_z \left[\frac{1}{m(z+a(t))}\right]_{\mu\nu} p_z + U_{\mu-\nu}(z) + v_{\mu\nu}(z) + \mu\omega\delta_{\mu\nu}. \tag{39}$$

In the diagonal term of $L_{\mu\mu}(z)$, the first term plays the role of a kinetic energy operator, and the remaining terms represent effective interactions. Here, $U_{\eta=0}(z)$ is generally considered to dominate $v_{\mu\mu}(z) = v_{00}(z)$ because the magnitude of the latter interaction is determined only by a relatively small variation in the effective mass of an electron over z. However, for a large value of F_{ac}, this would not always be the case. The last term of $\mu\omega$ with $\mu \neq 0$ contributes to PSB formation. Further, the off-diagonal term of $L_{\mu\nu(\neq\mu)}(z)$ is governed by $U_{\eta\neq0}(z)$ for the same reason as the diagonal one. Figure 2 shows the change in the diagonal term, $U_0(z)$, for α =1, 50, and $\alpha_{DL}^{(2,1)} = 108.2$. Here, the erosion of the potential barrier from $V(z)$ appears pronounced for larger values of α; $U_0(z)$ for $\alpha = 1$ is indistinguishable from $V(z)$. In particular, it is seen that the height of $U_0(z)$ at $\alpha = \alpha_{DL}^{(2,1)}$ is greater in the well region of $V(z)$ than that in the associated barrier region, unlike the height of $U_0(z)$ at $\alpha = 50$. Figure 3 shows the change in the off-diagonal term, $U_{\eta\neq0}(z)$, for $\alpha = 50$ and $\alpha_{DL}^{(2,1)}$ within the range of a single QW site. As α increases, $U_{\eta\neq0}(z)$ contributes more significantly to interactions between different channels even if $|\eta|$ is large, whereas $U_{\eta\neq0}(z)$ for $\alpha = 1$ almost vanishes; this is not shown here.

Based on the conventional Houston-Floquet picture, the photon-assisted tunneling (PAT) within the same miniband and ac-ZT across different minibands are responsible for diagonal and off-diagonal contributions of a dipole interaction of $F_1(t)z$, respectively. As shown in Fig. 1, it is understood that the DFR coupling is considered as a special case of ac-ZT intersubband coupling incorporating an approximately discrete DL state of (1,0) at $\alpha_{DL}^{(n,k)}$. On the other hand, in the RFT, the dominant interaction $U_\eta(z)$ of Eq. (38) incorporates the effects of both PAT and ac-ZT without any distinction between the two. Thus, it appears difficult to extract the effect of only ac-ZT from $U_\eta(z)$. The ac-ZT is partially induced by the ponderomotive potential $U_{\eta=0}(z)$ because this potential corresponds to the self-energy

of a DWSL electron that renormalizes the abovementioned off-diagonal dipole interaction.

In fact, the contribution of a decay caused by ac-ZT can be identified by examining the change in $\rho^{(ex)}(E)$ with respect to α. Without this coupling, the lifetime of a DWSL reflecting on $\rho^{(ex)}(E)$ would be responsible for the SR decay; it is considered that PAT would not affect the lifetime. In this case, the lifetime would be similar to that of a WSL, where SR is caused by dc-ZT because of a combined potential, $V(z) + F_0 z$, independently of α. Therefore, it is believed that the reduction in the lifetime of a DWSL relative to that of the associated WSL is attributable to ac-ZT. In the following, an interaction caused by the ponderomotive interaction $U_{\eta\neq 0}(z)$ is termed as interchannel coupling. Further, aside from the strict difference mentioned above between the ponderomotive interaction and ac-ZT, it is understood that this terminology is considered to have the same meaning as the intersubband coupling due to ac-ZT, unless otherwise stated.

C. Excess DOS with $n = 2$

Figure 4 shows the calculated results of $\rho^{(ex)}(E)$ for $\alpha = 1 \sim \alpha_{DL}^{(2,1)}$. $\rho^{(ex)}(E)$ for $\alpha = 1$ is almost identical to that of the WSL for $\alpha = 0$, where there exist four discernible peaks labeled as $(1, -1), (2, -2), (3, -3)$, and $(1, 0)$; the levels of $b = 1$ and 2 and the levels of $b \geq 3$ originate from the original QW levels below and above V_b, respectively. Here, the peaks for $b = 1$ are still stable [$T(E) \approx 4.3$ ps] despite the dc-ZT caused by the relatively large F_0, differing from the other two peaks for b =2 and 3 that appear blurred. This observation of the sharp peak for $b = 1$ is attributed to the fact that a potential drop in a well region of the QW (equal to $F_o d_w/2 = 1.9 \times 10^{-3}$, where d_w is the well width) is still smaller than V_b, and therefore, a tilted SL confining potential is capable of supporting the $b = 1$ level as an almost discrete one, namely, a sharp SR one. Moreover, because of this fact, it is also ensured that the DL level of $(1, j \neq 0)$ is assumed to be almost discrete because of the PSB of $(1, 0)$, as mentioned in Sec. I.

The variance of the peak positions for each b with respect to α is shown by connecting these positions by green solid lines. The pronounced anticrossing behavior between adjacent b's is seen around the specific α's, as indicated by the blue dotted ovals. Without the ponderomotive coupling, $U_{\eta\neq 0}(z)$, differing from the spectra in Fig. 4, no anticrossings manifest themselves, and the obtained peak positions appear only weakly dependent on α;

this is not shown here. However, the peak values of the $(1,-1)$ and $(1,0)$ levels without $U_{\eta\neq 0}(z)$ appear to be similar to those shown in Fig. 4. In addition to the anticrossings, a spike structures emerges at $\alpha = 30$, as indicated by the downward arrows. These structures are considered to be van Hove singularities that are common to conventional DWSL spectra. Here, the interchannel coupling due to ac-ZT would not yet be sufficiently strong to smear such detailed structures. As shown above, it is believed that the present RFT can reproduce anticrossings and the van Hove singularity in $\rho^{(ex)}(E)$ for relatively small α's, both of which feature the conventional model resorting to the two-miniband ac-ZT picture [50].

With a further increase in α from around $\alpha = 30$, $\rho^{(ex)}(E)$ is found to decrease rapidly, and the discernible peaks are overlapped and entangled with each other because of strong interchannel interactions; this leads to a difficulty in assigning each peak to an approximate quantum number (b, j). This tendency is pronounced at $\alpha = \alpha_{DL}^{(2,1)}$, and therefore, the associated $T(E)$'s of the blurred peaks decrease to a decay lifetime of approximately 120 fs. Further, a vestige of the collapse of the quasienergy miniband is no longer seen in the profile of $\rho^{(ex)}(E)$. This result is in sharp contrast to that of WSL at $\alpha = 1$. It is understood that such instability of DL is attributed to the DFR mechanism shown in Fig. 1; this is caused by ac-ZT-mediated interchannel coupling $U_\eta(z)$ between the energetically degenerate DL states, where one is the relatively stable state of $(1,0)$ and the other is the unstable continuum-like one of $(b > 1, j < 0)$.

It should be noted that the DFR differs from the conventional Fano effect in that sharp and blurred SR states are coupled via a dynamic interaction (namely, ac-ZT) in the former and discrete and continuum states are coupled via a static interaction (such as electron correlation) in the latter. Strictly speaking, FR is usually considered to be resonance caused by an interaction between closed and open channels, unlike the present DFR, in which there exists no closed channel, as mentioned in Sec. II A. The sharp SR state for DL is considered to be a quasi-closed channel. In the study of the autoionization of a negative hydrogen ion (H^-), it is known that FR is caused by an interchannel coupling similar to that of DFR, where the lowest doubly excited state of $(2s)(2p)\,{}^1P^o$ embedded in an SR continuum plays the role of this quasi-closed channel [51]. Therefore, it is considered that the DFR presented here is a new effect having both the *tunable* dynamic interaction and the *SR-mediated* FR as key roles, unlike conventional FR.

D. Excess DOS with $n = 1$

In order to deepen our understanding of the DFR mechanism, the F_0- and F_{ac}-dependence is examined by comparing the following three $\rho^{(ex)}(E)$'s for DL at $x_1^{(2)}, x_1^{(1)}$, and $x_2^{(1)}$, the traces of which are shown in Figs. 5, 6, and 7, respectively. $\rho^{(ex)}(E)$ in Fig. 5 is identical to that shown in Fig. 4 at $\alpha_{DL}^{(2,1)} = 108.2$ with $F_{ac} = 268.4$ kV/cm, $F_0 = 104.5$ kV/cm, and $\omega = 2.5 \times 10^{-3}$. With regard to $\rho^{(ex)}(E)$'s in Figs. 6 and 7 for $n = 1$, $F_0 = 52.3$ kV/cm, and hence, $\omega = 2.5 \times 10^{-3}$ are used in both cases, whereas $\alpha_{DL}^{(1,k)}$ $(k = 1, 2)$ values of $\alpha_{DL}^{(1,1)} = 80.7$ with $F_{ac} = 200.3$ kV/cm and $\alpha_{DL}^{(1,2)} = 147.8$ with $F_{ac} = 366.6$ kV/cm are adopted in the former and the latter, respectively. In these two $\rho^{(ex)}(E)$'s, it is assumed that the dominant peaks are ascribed to the DFR associated with the stable state of $(1, 0)$, in a manner similar to $\rho^{(ex)}(E)$ in Fig. 5. In fact, it would be necessary to confirm this speculation by tracking the peak positions corresponding to this DL state from $\alpha \approx 0$ to $\alpha = \alpha_{DL}^{(1,k)}$, as shown in Fig. 4.

In addition, the following two points should be noted with regard to Figs. 6 and 7. First, in Figs. 6 and 7, the peak height of $\rho^{(ex)}(\omega)$ at $\omega \approx -1.8 \times 10^{-3}$ does not appear to be identical to that at $\omega \approx 0.7 \times 10^{-3}$, contrary to the periodic relation given in Eq. (35). This is simply because of numerical errors. This periodic relation is of great importance in the evaluation of the accuracy of the calculations. One of the main causes of errors is presumably the difficulty in evaluating the ponderomotive interactions shown in Figs. 2 and 3 for a larger α with sufficient accuracy. In addition, the sector size of N adopted in actual calculations would be somewhat too sparse to satisfy this periodicity, although an increase in N from the adopted value would lead to a further increase in the calculations required. Next, in Fig. 7, the alternative mechanism of electron avalanche ionization (AI) [52, 53], described in Sec. III E, might become more important than the DFR at $F_{ac} = 366.6$ kV/cm. However, this is irrelevant here, because the purpose of analyzing Figs. 5–7 is to examine the dependence of $\rho^{(ex)}(\omega)$ on F_0 and F_{ac}, as shown below, and not to describe the criterion for the applicability of the DFR mechanism; this criterion is discussed in Sec. III E.

First, let the peak values in Figs. 6 and 7 be compared with that in Fig. 5, where F_0 in the former is only half that in the latter. The peak value in Fig. 6 (of the order of 7×10^4 a.u.) is greater than that in Fig. 5 (of the order of 3×10^4 a.u.). In particular, it should be noted that the peak value in Fig. 7 (of the order of 9×10^4 a.u.) is still greater than that in

Fig. 5 despite the much larger F_{ac} in the former. This observation appears to be compatible with the understanding based on Fig. 1 in that the width of the SR continuum arising from dc-ZT is reduced to a greater extent for smaller F_0, and therefore, the degeneracy with a quasienergy level of (1,0) is partially lifted, affording longevity to this DL state.

Next, the fact that the spectral patterns shown in Figs. 6 and 7 appear more involved than that shown in Fig. 5 is discussed. Before hypothesizing the reason for the difference between the resonant transitions with $n = 1$ and 2, it should be noted that the DL-quasienergy ε_{bj}, given by $\varepsilon_{bj} = \epsilon_b^{(c)} + j\omega$, is rewritten as

$$\varepsilon_{bj} = \epsilon_{bN_{wsl}} + \lambda\omega \tag{40}$$

within a single-miniband nearest-neighbor-tight-binding approximation, where $\epsilon_b^{(c)}$ is the center of the energy of the bth SL-miniband and $\epsilon_{bN_{wsl}}$ is a WSL energy level corresponding to the bth miniband with a WSL index $N_{wsl} = 0, \pm1, \pm2, \cdots$, namely, $\epsilon_{bN_{wsl}} = \epsilon_b^{(c)} + N_{wsl}\Omega$, and hence, $\lambda = j - nN_{wsl}$ is defined. This relation implies that the DL state with the quantum number (b, j) introduced in Sec. I consists of energetically degenerate WSL components labeled as $(b, [j, N_{wsl}])$. Such degeneracy results from the effect of PAT, because the WSL state with $N_{wsl} = 0$ is resonantly coupled with other states with $N_{wsl} \neq 0$ by successive n-photon emission/absorption. Strictly speaking, the WSL state with the $(b, [j, N_{wsl}])$ component is supported by a potential of $V_j^{(wsl)} \equiv V(z) + F_0 z + j\omega$. Hereafter, it is understood that this component is denoted as $[j, N_{wsl}]$ for the sake of simplicity, unless some ambiguity arises. Because of the PAT, the jth PSB is expressed as a linear combination of a set of bases with different $[j, N_{wsl}]$'s. For instance, for the PSBs of $(b, j = -1)$, there exists a degeneracy among the following components:

$$[j, N_{wsl}] = \cdots, [-1, -2], [-1, -1], [-1, 0], [-1, 1], \cdots. \tag{41}$$

With a decrease in F_{ac}, PAT is affected to a lesser extent, and therefore, it is considered that the PSB is governed by only a single component of $[j, 0]$ at the weak F_{ac} limit, because $\varepsilon_{bj} = \epsilon_{b,N_{wsl}=0} + j\omega$.

The first-order ac-ZT coupling primarily causes a transition between PSBs with (b, j) and $(b' \neq b, j' = j \pm 1)$, where $|j - j'| = 1$. With regard to a transition with $|j - j'| \geq 2$, such a higher-order coupling is negligibly small in a relatively weak F_{ac} region, whereas it becomes significant with an increase in F_{ac}, as mentioned in Sec. I. The DL state of $(1, 0)$, to which

the component of $[0,0]$ has a leading contribution, is likely coupled with another DL state of $(b \geq 2, -1)$ via ac-ZT. Here, it is believed that the dominant ac-ZT effect arises from the interaction between the two components of $(1,[0,0])$ and $(b \geq 2,[-1,0])$, because the overlap between these two with the same index as $N_{wsl} = 0$ usually has a large contribution. In the relatively weak F_{ac} region, it is evident that the PAT mediated by a single-photon resonant transition ($n = 1$) is more effective than that mediated by a two-photon one ($n = 2$). This results in stronger mixing among the WSL components of Eq. (41) for $n = 1$ as compared to that for $n = 2$. Therefore, it is theorized that for $n = 1$, the mixing of $(1,[0,0])$ with a great number of components of $(b \geq 2,[-1,N_{wsl}])$ by ac-ZT could give rise to the manifestation of various DL peaks in an entangled manner. On the other hand, for $n = 2$, it is believed that such an effect of ac-ZT is less pronounced, leading to the less involved structure of the spectra. Such a speculation could still be applied for interpreting the difference between the spectra shown in Figs. 6 and 7 and that shown in Fig. 5 for the region with a higher value of F_{ac}. With a further increase in F_{ac}, the spectral pattern could likely become more complicated irrespective of n, as long as many DL states are still discerned for relatively small F_0 without being blurred by the DFR.

In addition, as shown in Figs. 6 and 7, the lifetimes of both the dominant DL states appear comparable to each other despite the different F_{ac} applied. Moreover, both of the spectral patterns are similar. The reasons for the same are not yet evident, and hence, it would be necessary to track the peak positions of spectra from $\alpha \approx 0$ to $\alpha = \alpha_{DL}^{(1,k)}$.

E. Criteria for Applicability of DFR

Finally, two additional points are noted with regard to the present DFR mechanism. First, it is noted that the WSL resonance, namely, the dc-Zener resonance arising from the energy matching of WSL levels pertaining to different b's across some QW sites, has a pronounced effect on the width of the SR continuum at a particular value of F_0, represented here by F_0^* [54], because this gives rises to delocalization of a WSL electron. Therefore, the WSL resonance would cause irregular changes in the DFR lifetimes with respect to F_0 as an exception to the abovementioned observation of Figs. 5–7. In other words, it is likely that the DL state relevant to the WSL resonance at F_0^* decays more rapidly as compared to another DL state caused at F_0 that is greater than F_0^*, where F_{ac} is unchanged. In addition,

it is reported that the lifetimes of excitonic-WSL FR states exhibit such irregularity with respect to F_0 because of the WSL resonance [55].

Next, aside from the present DFR mechanism pertinent to a multiphoton process, it should be noted that there exists another mechanism for tunneling ionization (TI) [56] that possibly makes the DL unstable in the low-ω (low-F_0) region. TI is believed to be dominant in the region where $\gamma < 1$, where the Keldysh parameter γ is defined as

$$\gamma = \sqrt{\frac{V_b}{2U_p}}, \tag{42}$$

with the ponderomotive energy U_p equal to $F_{as}^2/4m_b\omega^2$. Equation (42) is rewritten as

$$\bar{F}_0 = \gamma F_{ac}, \tag{43}$$

where $\bar{F}_0$ is a scaled bias given by $\bar{F}_0 = F_0/[(2m_bV_b)^{1/2}d/n]$ and $\omega = F_0d/n$ has been used.

Figure 8 shows a scheme indicating the dominant regions of DFR and TI delimited by $\gamma = 1$, where the perturbation region denoted as P ($F_{ac} << 1$ and $\bar{F}_0 << 1$) and the multiple ionization region because of AI [52, 53] denoted as AI (($F_0 >> 1$ or $F_{ac} >> 1$) are also shown. γ corresponding to the DL at $x_k^{(n)}$ is given by

$$\gamma_k^{(n)} = \frac{(2m_bV_b)^{1/2}d}{x_k^{(n)}}. \tag{44}$$

Therefore, in the present system, the DL at $x_k^{(n)} > (2m_bV_b)^{1/2}d = 8.537$ would be considered unstable against TI, even if this DL is not affected by DFR. Following Fig. 8, it is found that for decays of DL states located at such higher $x_k^{(n)}$'s, the DFR mechanism presented here cannot be applied. For $n = 2$ in the case of Fig. 4, the first DL corresponding to $x_1^{(2)}$, namely, $\gamma_1^{(2)} = 1.662$, remains stable against TI, whereas the second DL is situated at around the boundary between DFR and TI because of $\gamma_2^{(2)} = 1.014$. Further, for $n = 1$ in the case of Figs. 6 and 7, both the first and the second DLs are considered to be stable against TI because of $\gamma_1^{(1)} = 2.223$ and $\gamma_2^{(1)} = 1.217$, respectively. These γ's are also indicated in Fig. 8. Generally, as F_{ac} increases with F_0 remaining unchanged, DL tends to become more unstable because of the TI mechanism rather than the DFR mechanism. In addition, it should be noted that for still larger F_0 and F_{ac}, AI is considered to dominate both DFR and TI, as shown in Fig. 8.

IV. CONCLUSION

It is revealed that the DL manifested in the DWSL is unstable against THz-mediated DFR coupling between the (1, 0) level and the quasienergetically degenerate levels of ($b > 1, j < 0$). This result is in sharp contrast to the conventional understanding of DL. Both the dynamic interaction and the SR-mediated FR play key roles in the DFR presented here, unlike conventional FR. The instability would be somewhat remedied by the reduction in F_0, aside from the TI mechanism. Therefore, it is speculated that in the dc-ZT-free system of the THz-driven SLs [57], the DL would not become unstable because of the DFR. Here, a continuum, into which a DL state is brought to decay, is no longer formed by the dc-ZT. On the other hand, the present DFR mechanism changes into another problem of a THz-driven SL-*exciton*, where an exciton level pertaining to one PSB is coupled with other PSBs as degenerated continua by both ac-ZT and an electron-hole Coulomb interaction, leading to FR decay [39]. Without ac-ZT, such excitonic DFR would not be caused. This differs from conventional SL and WSL excitons in that the concomitant FR decay exclusively arises from the Coulomb interaction [55]. The novel problem of excitonic DFR is now being investigated.

Acknowledgments

This work was supported by a Grant-in-Aid for Scientific Research on Innovative Areas "Optical science of dynamically correlated electrons (DYCE)" (No. 21104504) of the Ministry of Education, Culture, Sports, Science and Technology (MEXT), Japan.

---

[1] K. Sakai (Ed.), *Terahertz Optoelectronics*, (Springer-Verlag, Berlin, 2005).

[2] S. D. Ganichev and W. Prettl, *Intense Tetahertz Excitation of Semiconductors*, (Oxford University Press, 2006).

[3] B. Bartal, I. Z. Kozma, A. G. Stepanov, G. Almási, J. Kuhl, E. Riedle, and J. Hebling, Appl. Phys. B **86**, 419 (2007).

[4] N. Karpowicz, J. Dai, X. Lu, Y. Chen, M. Yamaguchi, L. Zhang, C. Zhang, M. Price-Gallagher, C. Fletcher, O. Mamer, A. Lesimple, and K. Johnson, Appl. Phys. Lett. **92**, 011131 (2008).

[5] S. Kohler, J. Lehmann, and P. Hänggi, Phys. Rep. **406**, 379 (2005).

[6] M. Holthaus, Phys. Rev. Lett. **69**, 351 (1992).

[7] J. Zak, Phys. Rev. Lett. **71**, 2623 (1993).

[8] K. Yashima, K. Hino, and N. Toshima, Phys. Rev. B **68**, 235325 (2003).

[9] R. B. Liu and B. F. Zhu, Phys. Rev. B **59**, 5759 (1999).

[10] D. R. Hofstadter, Phys. Rev. B **14**, 2239 (1976).

[11] F. Grossmann, T. Dittrich, P. Jung, and P. Hänggi, Phys. Rev. Lett. **67**, 516 (1991).

[12] M. Grifoni and P. Hänggi, Phys. Rep. **304**, 229 (1998), and references cited therein.

[13] Y. Kayanuma and K. Saito, Phys. Rev. A **77**, 010101(R) (2008).

[14] K. -H. Ahn, H. C. Park, and B. Wu, Physica E **34**, 468 (2006).

[15] E. Papp, C. Micu, and L. Aur, Superlattices and Microstructures **44**, 770 (2008).

[16] K. W. Madison, M. C. Fischer, and M. G. Raizen, Phys. Rev. A **60**, R1767 (1999).

[17] S. Haroche, C. Cohen-Tannoudji, C. Audoin, and J. P. Schermann, Phys. Rev. Lett. **24**, 861 (1970).

[18] G. Xu and D. J. Heinzen, Phys. Rev. A **59**, R922 (1999).

[19] T. Shirahama, X. M. Tong, K. Hino, and N. Toshima, Phys. Rev. A **80**, 043414 (2009).

[20] J. Karczmarek, M. Stott, and M. Ivanov, Phys. Rev. A **60**, R4225 (1999).

[21] M. Glück, A. R. Kolovsky, and H. J. Korsch, Phys. Rep. **366**, 103 (2002).

[22] A. Eckardt, C. Weiss, and M. Holthaus, Phys. Rev. Lett. **95**, 260404 (2005).

[23] M. Sillanpää, T. Lehtinen, A. Paila, Y. Makhlin, and P. Hakonen, Phys. Rev. Lett. **96**, 187002 (2006).

[24] N. Tsuji, T. Oka, and H. Aoki, Phys. Rev. B **78**, 235124 (2008).

[25] M. Holthaus and D. W. Hone, Philosophical Magazine B **74**, 105 (1996).

[26] K. Hino, K. Yashima, and N. Toshima, Phys. Rev. B **71**, 115325 (2005).

[27] U. Fano, Phys. Rev. **124**, 1866 (1961).

[28] J. Z. Tang, S. Watanabe, and M. Matsuzawa, Phys. Rev. A **46**, 2437 (1992).

[29] F. Cerdeira, T. A. Fjeldly, and M. Cardona, Phys. Rev. B **8**, 4734 (1973).

[30] P. L. Knight, M. A. Lauder, and B. J. Dalton, Phys. Rep. **90**, 1 (1990).

[31] J. L. Bohn and P. S. Julienne, Phys. Rev. A **56**, 1486 (1997).

[32] R. Ciurylo, E. Tiesinga, and P. S. Julienne, Phys. Rev. A **74**, 022710 (2006).

[33] K. Enomoto, K. Kasa, M. Kitagawa, and Y. Takahashi, Phys. Rev. Lett. **101**, 203201 (2008).

[34] J. Purvis, M. Dörr, M. Terao-Dunseath, C. J. Joachain, P. G. Burke, and C. J. Noble, Phys.

Rev. Lett. **71**, 3943 (1993), and references cited therein.

[35] F. T. Smith, Phys. Rev. **118**, 349 (1960).

[36] R. Balian and C. Bloch, Annals of Physics **60**, 401 (1970).

[37] J. L. Kinsey, Chem. Phys. Lett. **8**, 349 (1971).

[38] M. Desouter-Lecomte and X. Chapuisat, Phys. Chem. Chem. Phys. **1**, 2635 (1999), and references cited therein.

[39] N. Maeshima, D. Misaki, and K. Hino (unpublished).

[40] R. -B. Liu and B. -F. Zhu, J. Phys.: Condens. Matter **12**, L741 (2000).

[41] K. Hino, K. Goto, and N. Toshima, Phys. Rev. B **69**, 035322 (2004).

[42] M. Kroner, A. O. Govorov, S. Remi, B. Biedermann, S. Seidl, A. Badolato, P. M. Petroff, W. Zhang, R. Barbour, B. D. Gerardot, R. J. Warburton, and K. Karrai, Nature **451**, 311 (2008).

[43] M. V. Fedorov and A. E. Kazakov, Prog. Quantum Electron. **13**, 1 (1989).

[44] Z. Deng and J. H. Eberly, Phys. Rev. A **36**, 2750 (1987).

[45] H. Hirori, M. Nagai, and K. Tanaka, Phys. Rev. B **81**, 081305(R) (2010).

[46] W. C. Henneberger, Phys. Rev. Lett. **21**, 838 (1968).

[47] J. C. Light, I. P. Hamilton, and J. V. Lill, J. Chem. Phys. **82**, 1400 (1985).

[48] K. Hino, T. Ishihara, F. Shimizu, N. Toshima, and J. H. McGuire, Phys. Rev. A **48**, 1271 (1993).

[49] K. Hino, J. Phys. Soc. Jpn. **67**, 3159 (1998).

[50] K. Hino, X. M. Tong, and N. Toshima, Phys. Rev. B **77**, 045322 (2008).

[51] K. Hino, M. Nagase, H. Okamoto, T. Morishita, M. Matsuzawa, and M. Kimura, Phys. Rev. A **49**, 3753 (1994).

[52] G. Juska and K. Arlauskas, Phys. Stat. Sol. (a) **59**, 389 (1980).

[53] M. N. Shneider, Z. Zhang, and R. B. Miles, J. Appl. Phys. **104**, 023302 (2008).

[54] H. Schneider, H. T. Grahn, K. von Klizting, and K. Ploog, Phys. Rev. Lett. **65**, 2720 (1990).

[55] K. Hino, and N. Toshima, Phys. Rev. B **71**, 205326 (2005), and references cited therein.

[56] M. V. Ammosov. N. B. Delone, and V. P. Krainov, Sov. Phys. JETP **64**, 1191 (1986).

[57] J. Rotvig, A. -P. Jauho, and H. Smith, Phys. Rev. Lett. **74**, 1831 (1995); Phys. Rev. B **54**, 17691 (1996).

TABLE I: Summary of acronyms used in text in alphabetical order and corresponding meanings.

acronyms	meanings
AI	avalanche ionization
DFR	dynamic Fano resonance
DL	dynamic localization
DOS	density of state
DWSL	dynamic WSL
FR	Fano resonance
KH	Kramers-Henneberger
MCS	multichannel scattering
PAT	photon-assisted tunneling
PSB	photon sideband
QW	quantum well
RFT	R-matrix Floquet theory
SL	superlattice
SR	shape resonance
TI	tunneling ionization
WSL	Wannier-Stark ladder
ZT	Zener tunneling

FIG. 1: Schematic diagram showing DL manifold and DFR mechanism between DL levels. Each level is shaded depending on degree of magnitude of SR. For more detail, consult text.

FIG. 3: Ponderomotive couplings $U_\eta(z)$ ($\eta = 1 \sim 5$) as a function of z-coordinate (a.u.) within a single QW site for $\alpha = 50$ [in panel (a)] and $108.2(= \alpha_{DL}^{(2,1)})$ [in panel (b)]. Here, $U_\eta(z)$ with $\eta =$ 1, 2, 3, 4, and 5 are indicated by red, green, blue , purple, and black solid lines, respectively.

FIG. 2: Ponderomotive potential $U_0(z)$ as a function of z-coordinate for $\alpha = 1$, 50, and $108.2(= \alpha_{DL}^{(2,1)})$ indicated by black, blue, and red solid lines, respectively. Here, $F_0 = 104.5$ kV/cm.

FIG. 4: Excess DOS, $\rho^{(ex)}(E)$, as a function of quasienergy E in range of $\alpha = 1 \sim 108.2(= \alpha_{DL}^{(2,1)})$. Curves are shifted for clarity. Four discernible peaks are assigned to approximate quantum numbers (b, j); each peak attributable to the same (b, j) is connected by solid green lines and some prominent anticrossings are indicated by blue chain ovals. Further, at $\alpha = 30$, spike structures corresponding to van Hove singularities for the (1,0) peak are indicated by downward arrows. Here, $F_0 = 104.5$ kV/cm and $\omega = 2.5 \times 10^{-3}$.

FIG. 5: Excess DOS, $\rho^{(ex)}(E)$, as a function of quasienergy E at $\alpha_{DL}^{(2,1)} = 108.2$ with $F_{ac} = 268.4$ kV/cm, $F_0 = 104.5$ kV/cm, and $\omega = 2.5 \times 10^{-3}$.

FIG. 6: Same as Fig. 5 but at $\alpha_{DL}^{(1,1)} = 80.7$ with $F_{ac} = 200.3$ kV/cm, $F_0 = 52.3$ kV/cm, and $\omega = 2.5 \times 10^{-3}$.

FIG. 7: Same as Fig. 5 but at $\alpha_{DL}^{(1,2)} = 147.8$ with $F_{ac} = 366.6$ kV/cm, $F_0 = 52.3$ kV/cm, and $\omega = 2.5 \times 10^{-3}$.

FIG. 8: Traces of $\bar{F}_0$ as a function of F_{ac} following the relation of Eq. (43) for $\gamma = \gamma_1^{(1)}$ (red line), $\gamma_1^{(2)}$ (blue line), $\gamma_2^{(1)}$ (green line), and $\gamma_2^{(2)}$ (purple line). Two regions governed by DFR and TI are delimited by $\gamma = 1$ (black line). Perturbation region, denoted as P, and avalanche ionization region, denoted as AI, are also shown.

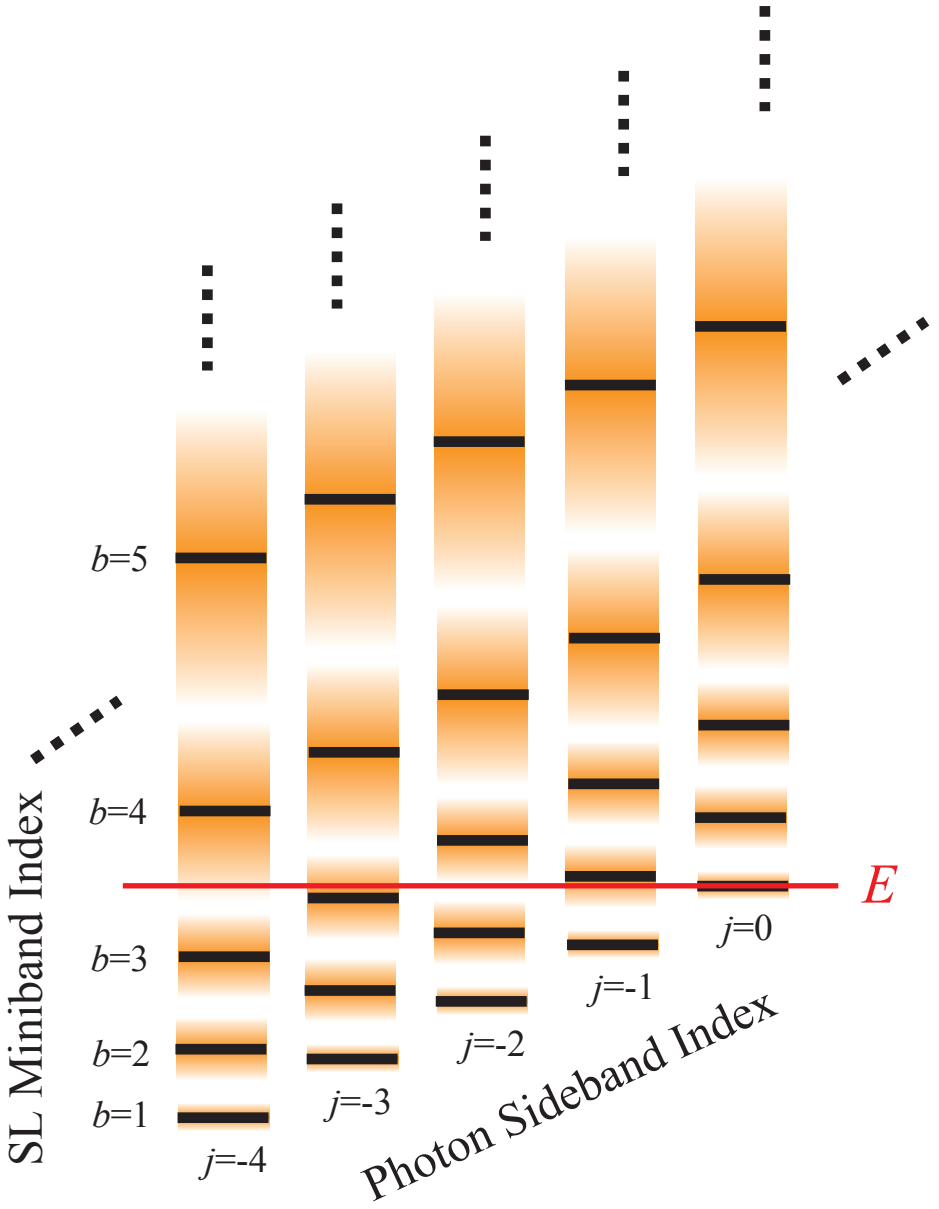
SL Miniband Index
b=5
b=4
b=3
b=2
b=1
E
j=-4
j=-3
j=-2
j=-1
j=0
Photon Sideband Index

Fig. 1

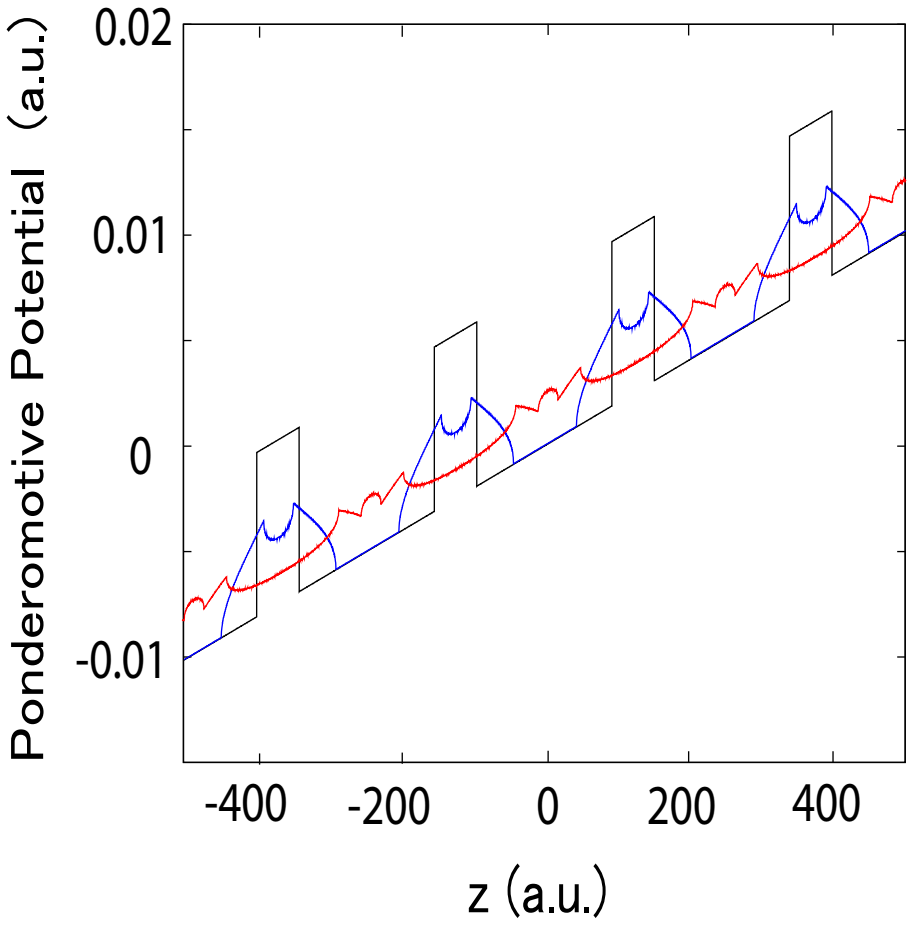
Ponderomotive Potential (a.u.)
0.02
0.01
0
-0.01
-400
-200
0
200
400
z (a.u.)

Fig. 2

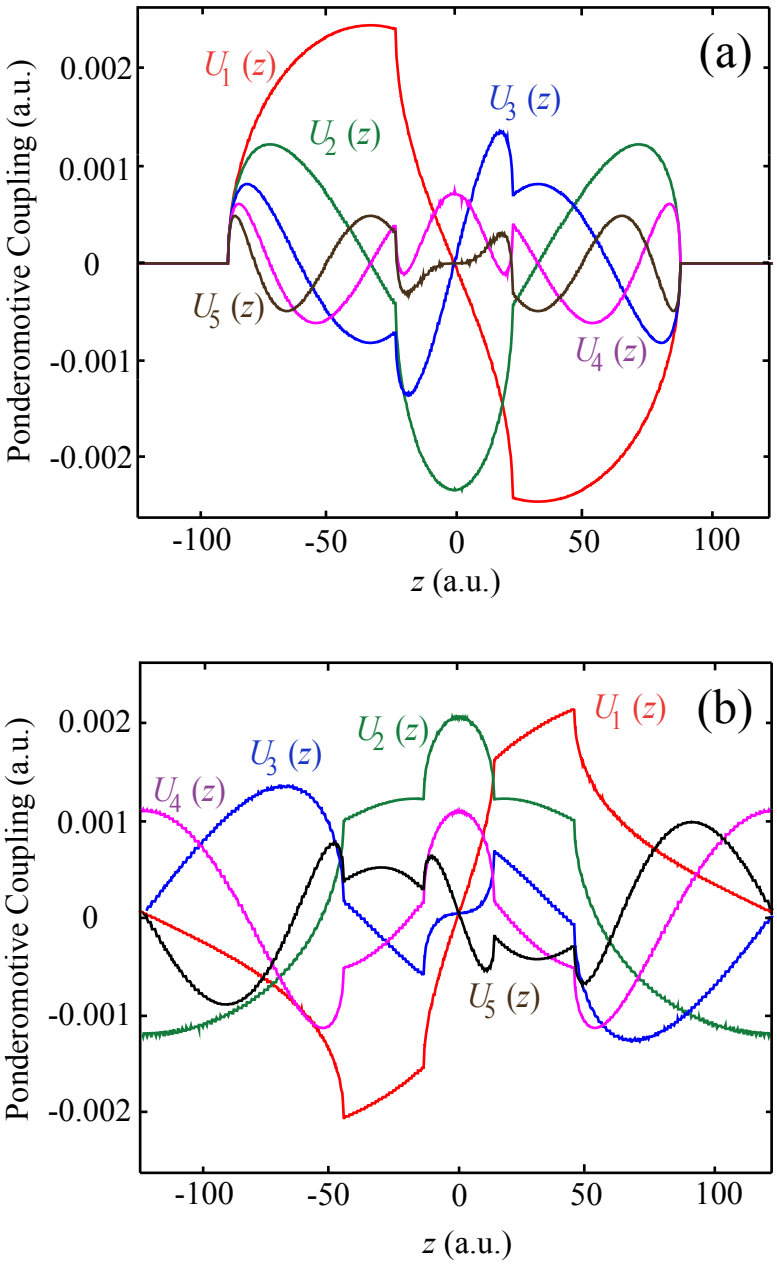
(a)
$U_1(z)$
$U_2(z)$
$U_3(z)$
$U_4(z)$
$U_5(z)$
Ponderomotive Coupling (a.u.)
0.002
0.001
0
-0.001
-0.002
-100
-50
0
50
100
z (a.u.)
(b)
$U_1(z)$
$U_2(z)$
$U_3(z)$
$U_4(z)$
$U_5(z)$
Ponderomotive Coupling (a.u.)
0.002
0.001
0
-0.001
-0.002
-100
-50
0
50
100
z (a.u.)

Fig. 3

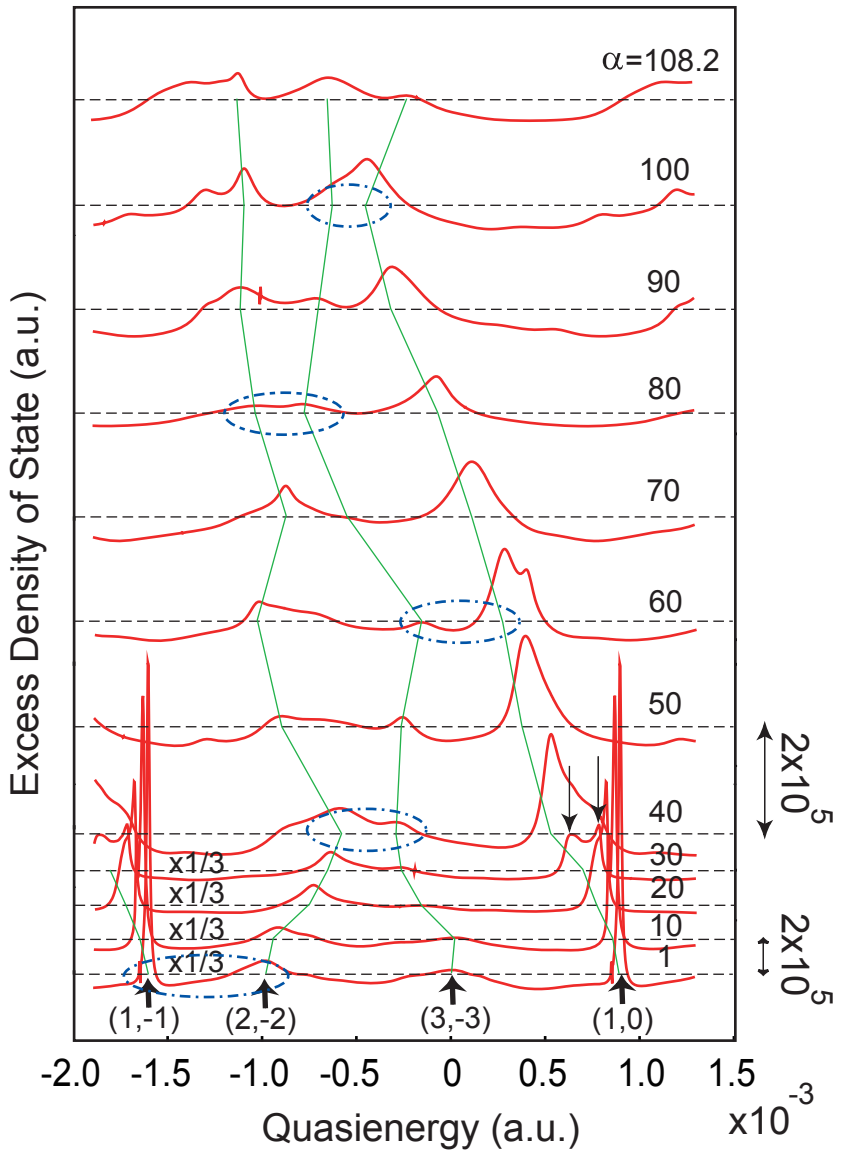
α=108.2
100
90
80
70
60
50
40
30
20
10
1
x1/3
x1/3
x1/3
x1/3
(1,-1)
(2,-2)
(3,-3)
(1,0)
2x10^5
2x10^5
Excess Density of State (a.u.)
-2.0
-1.5
-1.0
-0.5
0
0.5
1.0
1.5
Quasienergy (a.u.)
x10^-3

Fig. 4

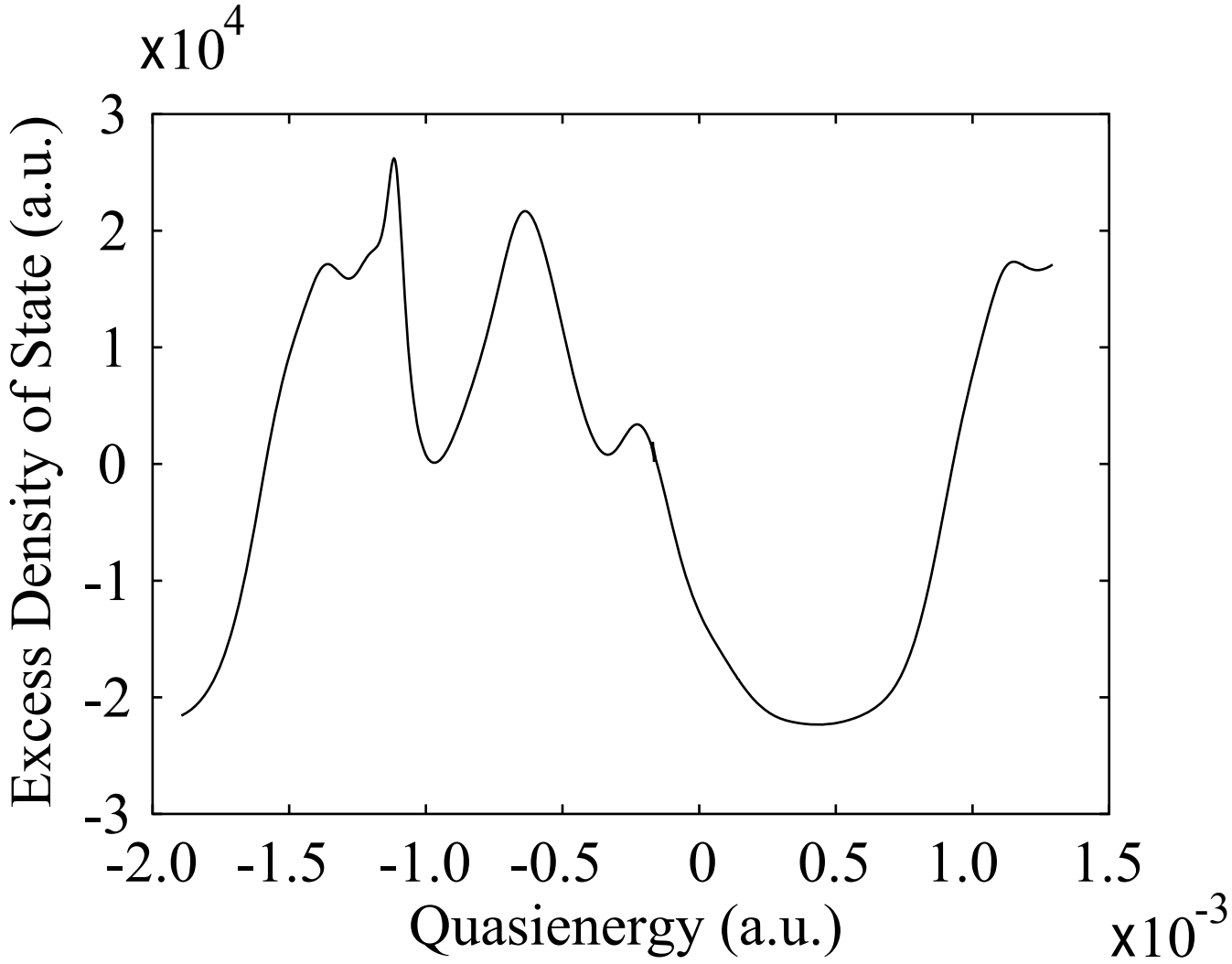
x10^4
3
2
1
0
-1
-2
-3
Excess Density of State (a.u.)
-2.0
-1.5
-1.0
-0.5
0
0.5
1.0
1.5
Quasienergy (a.u.)
x10^-3

Fig. 5

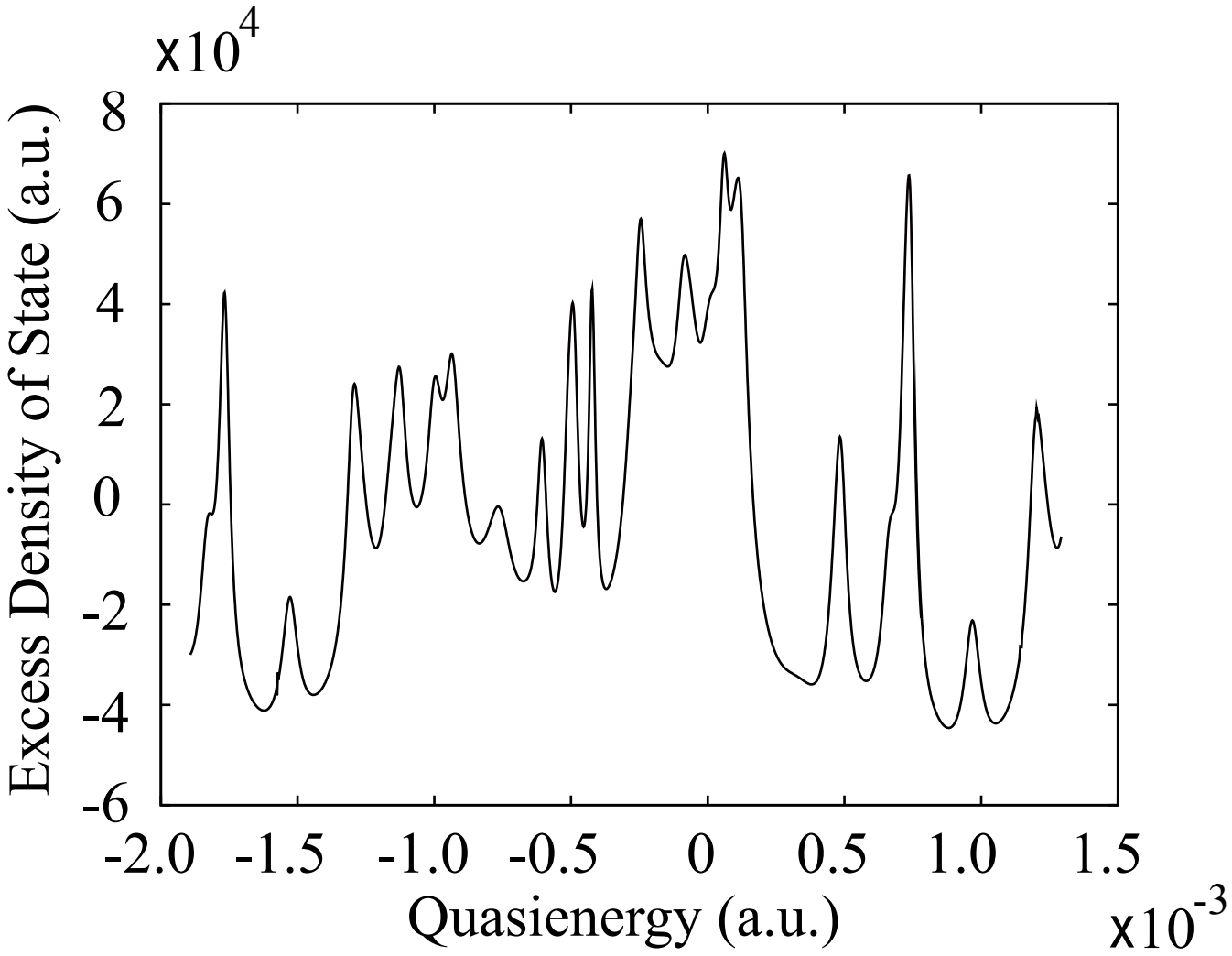
x10^4
8
6
4
2
0
-2
-4
-6
Excess Density of State (a.u.)
-2.0
-1.5
-1.0
-0.5
0
0.5
1.0
1.5
Quasienergy (a.u.)
x10^-3

Fig. 6

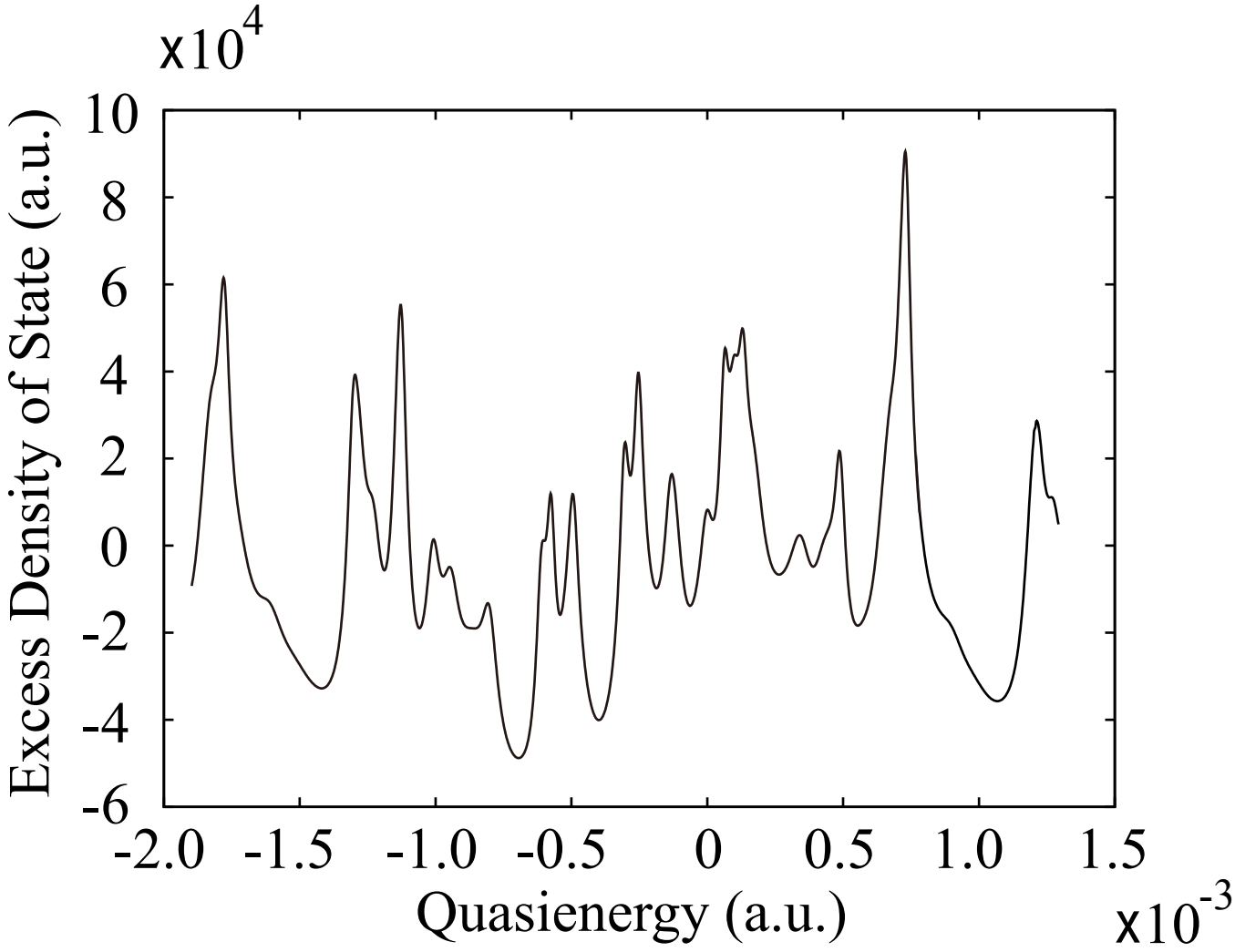
x10^4
10
8
6
4
2
0
-2
-4
-6
Excess Density of State (a.u.)
-2.0
-1.5
-1.0
-0.5
0
0.5
1.0
1.5
Quasienergy (a.u.)
x10^-3

Fig. 7

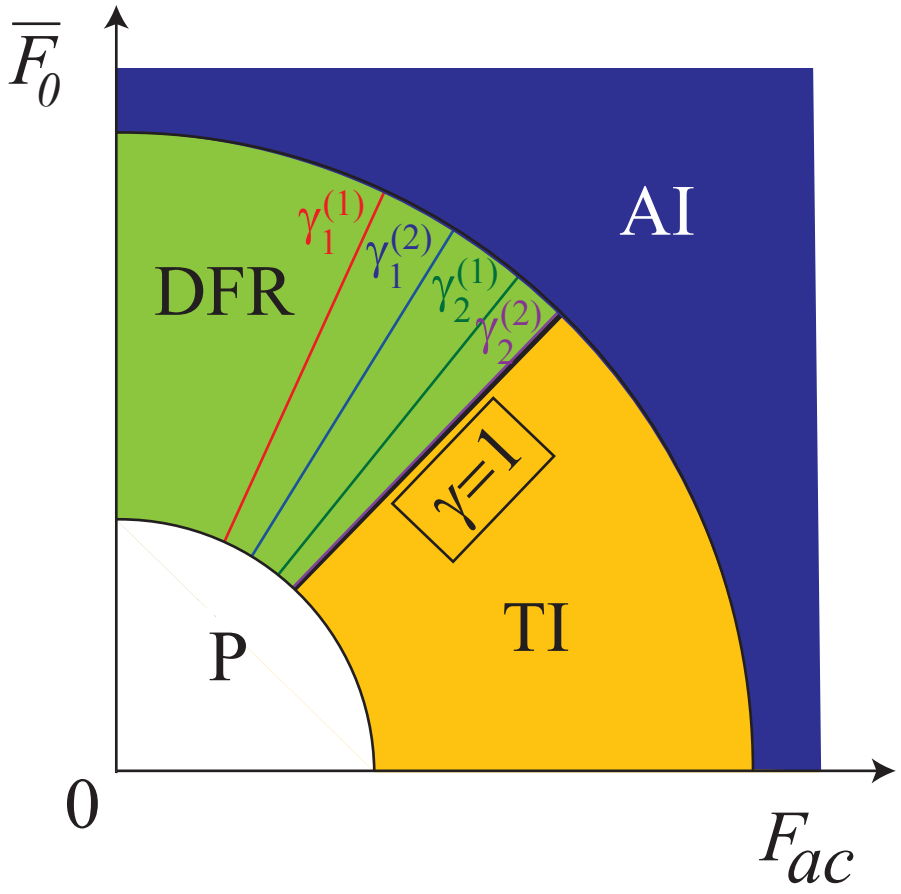
$\overline{F_0}$
AI
DFR
$\gamma_1^{(1)}$
$\gamma_1^{(2)}$
$\gamma_2^{(1)}$
$\gamma_2^{(2)}$
γ=1
TI
P
0
F_{ac}

Fig. 8